*metals*

MDPI

*Article*

# Numerical Simulations of Stress Intensity Factors and Fatigue Life in L-Shaped Sheet Profiles

**Ferdinand Dömling *, Florian Paysan and Eric Breitbarth**

Institute of Materials Research, German Aerospace Center (DLR), Linder Höhe, 51147 Köln, Germany; florian.paysan@dlr.de (F.P.); eric.breitbarth@dlr.de (E.B.)
* Correspondence: ferdinand.doemling@dlr.de

**Abstract:** The assessment of fatigue cracks is an elementary part of the design process of lightweight structures subject to operational loads. Although angled sheets are standard components in forming technology, fatigue crack growth in geometries like C- and L-sections has been little-studied and is mostly limited to crack growth before the transition through the corner. In this study, fatigue crack propagation is simulated to explore the influence of sheet thickness, corner angle and corner radius on the fatigue life in an L-section. The stress intensity factor (SIF) is derived as the driving force of crack growth over the full crack path. Special attention is paid to the evolution of the SIF in the radius sub-section and its implications on the fatigue life. The results show that the SIF in an angled sheet for given loading conditions and crack lengths cannot be readily approximated by the SIF in an equivalent straightened sheet. The bending angle and radius lead to crack growth retardation or acceleration effects. These findings are important for the design and optimization of forming geometries with regard to fatigue crack growth.

**Keywords:** stress intensity factor; L-section; finite element simulation; fatigue crack growth; fracture mechanics

check for updates

**Citation:** Dömling, F.; Paysan, F.; Breitbarth, E. Numerical Simulations of Stress Intensity Factors and Fatigue Life in L-Shaped Sheet Profiles. *Metals* **2024**, *14*, 1463. https://doi.org/10.3390/met14121463

Academic Editor: Alberto Campagnolo

Received: 22 November 2024
Revised: 12 December 2024
Accepted: 18 December 2024
Published: 21 December 2024



## 1. Introduction

Metal fatigue remains a major concern in engineering structures subjected to variable cyclic loading. Findlay and Harrison [1] argued that, for aircraft components in particular, the majority of failures (55%) can be attributed to fatigue, while in general engineering applications, fatigue still accounts for 25%, second only to corrosion.

With a shift in industry towards increased sustainability [2,3], new and optimized manufacturing processes for lightweight components [4–7] might offer enhanced performance capabilities, greater design freedom and significant benefits in terms of resource efficiency. From the perspective of damage tolerance [8], the close relationship between manufacturing processes and fatigue properties [9–12] requires a reassessment of crack growth behaviour in critical applications. The required extensive test program is often time-consuming and costly [13]. An accurate numerical model including manufacturing-related variables of fatigue crack growth in complex real-world structures enables smaller safety factors and further reduces component weights and costs.

While the modeling of fatigue in virtual testing [14–17] has the potential to accelerate the implementation of optimized components, it also requires a more profound understanding of the relevant geometrical- and materials processing-related factors and their interconnections. Therefore, effects like microstructure formation [18–20], cold hardening [21–25], residual stress [26–28] and manufacturing-related damage [29–32] are of particular significance in the processed zone of the component. This section may not only exhibit significant deviations on a micromechanical level but also geometric differences from the samples employed in laboratory experiments.

Recently, the high-fidelity experimental evaluation of fatigue properties in geometries closer to real components has come into focus, combining optical and analytical methods.

Mokhtarishirazabad et al. [33] present a hybrid optical–analytical approach, combining digital image correlation (DIC) with modeling the linear–elastic field around the crack tip via the Williams series' expansion approximation. Vormwald et al. [34] investigate mixed-mode fatigue in thin-walled tubes using DIC. Similarly to Mokhtarishirazabad et al., they bypass the issue of DIC on curved surfaces through high magnification, ensuring a locally flat plate approximation. Camacho-Reyes et al. [35] propose a differential geometry method combined with 3D-DIC to characterize crack tip fields on non-planar surfaces, extending 2D models to 3D developable surfaces. Cao and Sipos [36] introduce a novel approach to the determine stress intensity factors of cylinders and domes by adapting the Williams expansion to non-developable surfaces. All studies emphasize the importance of advanced experimental techniques, in conjunction with analytical models, to better understand crack behaviour in more complex geometries and loading conditions beyond traditional planar assumptions.

Even for a cross-section of standard three-dimensional (3D) engineering geometries, such as angled sheets with I-, T-, C- and circular cross-sections (exemplarily [37–42]), there is a lack of available analytical handbook solutions of varying accuracies that are readily available for comparison with experimental data. These geometries are commonly encountered in structural components such as stiffened plates used in aerospace, marine and civil engineering applications, where understanding crack arrest behavior and fatigue performance is crucial. Stiffener-plate configurations and residual stresses significantly influence crack propagation and arrest mechanisms in these structures. For instance, Huang et al. [43] showed that intact stiffeners enhance crack arrest effects, but the performance diminishes rapidly once stiffeners are compromised. Llopart et al. [44] found that certain stringer geometries are more suitable than others to reduce stress intensity factors and improve fatigue life. Labeas et al. [45] observed that residual stresses from welding processes can reduce SIFs, particularly with laser beam welding compared to high-speed machining, emphasizing the role of the manufacturing route.

Since an arbitrary curved crack front is not readily parameterizable, however, such solutions are often limited to straight crack fronts and/ or restricted to cracks before and after transitioning through the corner regions of respective geometries. In order to fill this gap in understanding the fundamental behavior of cracks in such geometries, a parameterized finite element (FE) study was utilized to identify the effect of specimen geometry on the stress intensity factor (SIF) of a single edge crack in a partially curved sheet under cyclic loading. Given that advanced sheet metal bending offers a cost-effective and efficient method for producing lightweight components, a bending geometry was adopted to mirror practical manufacturing techniques. The focus was on the crack growth stage and an efficient adaptive remeshing approach was used to derive the crack-front shape step-by-step. The design space considered the sheet thickness, the bending angle and the bending radius. The focus was on the L-profile shape and the effect of the bending angle on the geometry of the crack front and the SIF is described. The degrees of freedom of the model were confined realistically to represent a conductible laboratory experiment under a uniaxial load. By comparing the SIF of an equivalent crack in a straight sheet, the deviation in the crack's SIF due to the bending angle and radius was quantified. Furthermore, geometries that were adapted to specific design cases are presented. The focus was on the radius for an angle of 90° and constant thickness as it had the least impact on functionality and was mainly influenced by the design and the manufacturing process. Then, the expected lifetime for exemplary components mapped from the parameters' space was estimated and the implications of the findings on the lifetime of a part with a variable bending radius are discussed. Finally, design and evaluation insights to further improve component life are provided.

## 2. Materials and Methods

This finite element parameter study was performed using the ANSYS multi-physics solver MAPDL 22.2 (ANSYS Inc.; Canonsburg, PA, USA) with a Linux workstation (2x

Intel Xeon Gold 6240 18C, 256 GB RAM, NVIDIA RTX8000). The simulation workflow was implemented in PyANSYS [46] (v0.64.0). PyANSYS is a Python API for communicating with the Mechanical Ansys Parametric Design Language (MAPDL) instance. This approach allowed us to leverage the general expressiveness of the Python language while maintaining the computational efficiency of the MAPDL core.

In this study, the influence of three geometrical parameters on the evolution of the SIF in the model of a sheet pre-product under axial loading was investigated. The key input parameters considered were the sheet thickness, t, bending angle, $\alpha$, and bending radius, r. The parameter spaces are listed in Table 1.

**Table 1.** Examined parameter variation in a total of 126 3D crack growth simulations with a constant width of straight sections of $W_{pre}$ = $W_{post}$ = 50 mm (V1_WPrePost). An additional 5 simulations were conducted with t = 4 mm and $\alpha$ = 90° and variational r with a constant total sample width, W (V2_WTotal), and an additional 5 were conducted with a constant bounding box (V3_BBox). As a reference, for each parameter variation, an additional 2D simulation of a straight sheet with an equal width, W = 181 mm, was conducted.

| Parameter | Symbol | V1_WPrePost | V2_WTotal | V3_BBox |
|---|---|---|---|---|
| Sheet thickness | t | [2,4,8] mm | 4 mm | |
| Bending angle | $\alpha$ | [5,10,20,40,60,90,120]° + straight sheet ($\alpha$ = 0 °) | 90° + straight sheet ($\alpha$ = 0 °) | |
| Bending radius | r | [5,10,20,30,50] mm + L-profile (r = 0 mm) | | |

Figure 1a,b show a schematic model of the parameterized bended sheet for a special case of the standard L-profile with a bending angle of $\alpha$ = 90° and bending radius of r = 0 mm.

In the y-direction, the length L equaled 400 mm and was chosen to be constant for all parameter sets. Since the model's base was an isosceles, the web and flange were of the same geometry. To distinguish the individual sections, the equivalent width W of the model was divided into 3 parts: (1) the pre-corner section ($W_{pre}$) with the initial notch (artificial crack), (2) the corner section ($W_{corner}$) with the radius and (3) the post-corner section ($W_{post}$). The nomenclature followed the expected crack growth direction in the x-dimension. Figure 1c depicts the corner region and the crack-front descriptors, including two measures of the crack-front width. Here, $c^{ins,out}$ was the distance between the endpoints of the crack front on the inside and outside of the profile and the Euclidean distance between each crack-front node, $\Delta c^{node}$, as a summand of the total Euclidean crack-front width, $c_{cf} = \sum \Delta c^{node}$, as also shown in Figure 1c. The crack-front depth, $d_{cf}$, was the maximum perpendicular distance from the segment represented by $c^{ins,out}$ and provided inside into the crack front's curvature. Figure 1d provides an exemplar of the final three-dimensional geometric model for the parameters r $\neq$ 0 mm and $\alpha \neq 90°$.

For the pre- and post-corner section, three variations were chosen: The first variant (hereinafter referred to as 'V1_WPrePost') kept the widths $W_{pre}$ = $W_{post}$ = 50 mm constant over all parameter sets. The total width, $W_{total} = W_{pre} + W_{corner} + W_{post}$, was then fully defined by the addition of the neutral fibre increment $W_{corner} = f(\alpha, r, t)$, equal to $\frac{\alpha\pi}{180°}\left(r + \frac{t}{2}\right)$ for r > 0 and $\tan\left(\frac{\alpha}{2}\right)$t t for r = 0. This version of the angled sheet was fully parameterized over $\alpha$, r and t.

The second variant (hereinafter referred to as 'V2_WTotal') considered, from the design perspective, the specific application of an L-shaped component with a constant width (W = 181 mm) and variable radius. For this special case, $\alpha$ = 90° and t = 4 mm were kept constant and $W_{pre} = W_{post} = (W_{total} - W_{corner})/2$ as a function of r. In general, the bending radius, r, was the radius at the root of the corner. The outer radius, r + t, followed the shape at the root's radius.

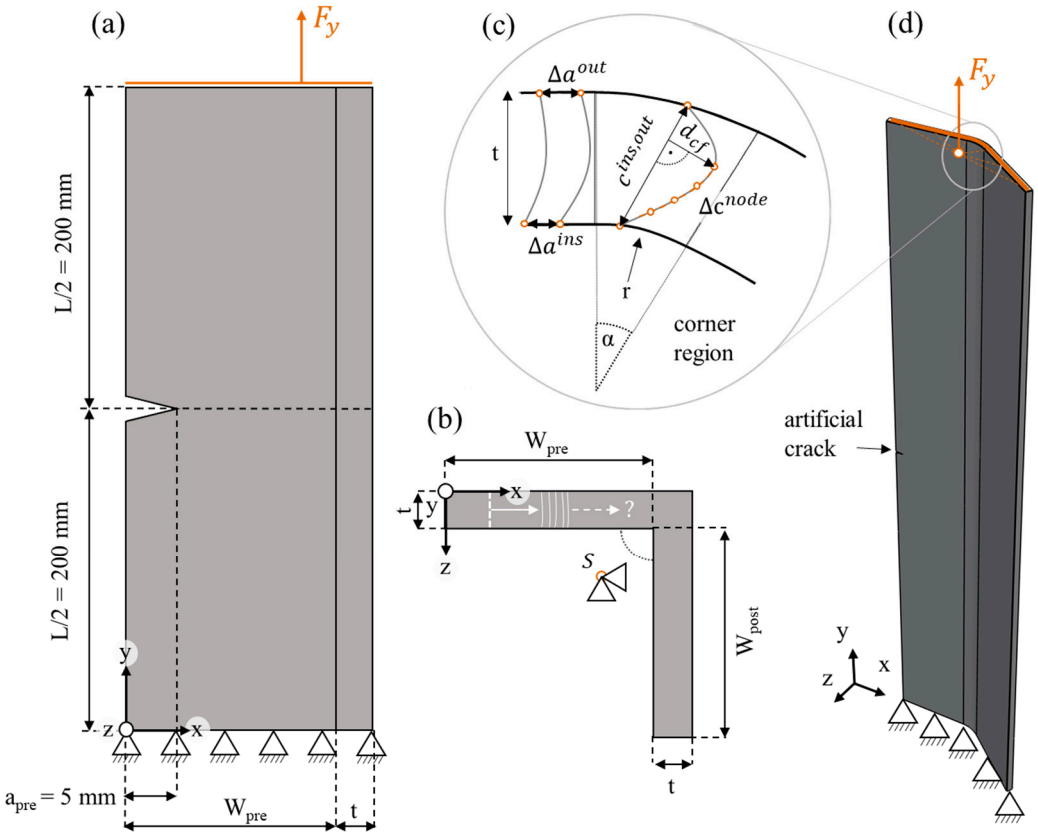


**Figure 1.** Exemplary models of the angled sheet with applied boundary conditions. (**a**) Schematic for α = 90° and r = 0 (L-profile) with a front view and (**b**) top view. (**c**) A corner region with geometric parameters and crack-front descriptors (**d**) Three-dimensional geometry with an isometric view for t = 4 mm; α = 40°; and r = 20.

The third variant (hereinafter referred to as 'V3_BBox') addressed the design perspective with a focus on maintaining a constant installation space. In this scenario, the total width, $W_{total}$, was a function of α and r, similarly to the geometry considerations for a constant leg width. However, $W_{total}$ was inversely proportional to both α and r: $W_{total} \propto \alpha^{-1}, r^{-1}$. Like in V2_WTOTAL, α was kept constant at 90°. This relationship meant, in general, that a smaller bending radius allowed for a better approximation of the installation space contour, leading to a higher overall sheet width for smaller radii. This design variant would provide a more efficient use of the available space, particularly advantageous in applications where space constraints are critical. As the starting geometry for crack growth, the initial notch of the length $a_{pre}$ = 5 mm was placed centered at (x,y) = (0, 200) mm. The "artificial crack" acted as an initial flaw and was oriented for pure mode-I loading.

Figure 2 shows examples of V1_WPrePost, V2_WTotal and V3_BBox.

The boundary conditions were defined as shown in Figures 1 and 3. The lower end (y = 0 mm) of the model was fixed (APDL command: D,ALL,ALL,0) in all three spatial directions. Mechanical uniform loading was applied via remote loading, implemented through a multi-point constraint using ANSYS TARGE170 and CONTA174 elements at the upper end (y = 400 mm). The remote point's coordinates corresponded to the centroid of the uncracked section. The centroid of the uncracked section, which was identical to the base area, was derived via tessellation (APDL command: ASUM) for each parameter set. The loading axis remained constant over the virtual crack growth experiment and was not affected by the crack length, ensuring that it did not change as the uncracked ligament decreased during crack growth. A remote point was used for loading to simplify the modeling process by replacing a more complex guided linear motion system, e.g.,

the clamping system of a testing rig, thereby ensuring an accurate representation of load transfer while maintaining computational efficiency.

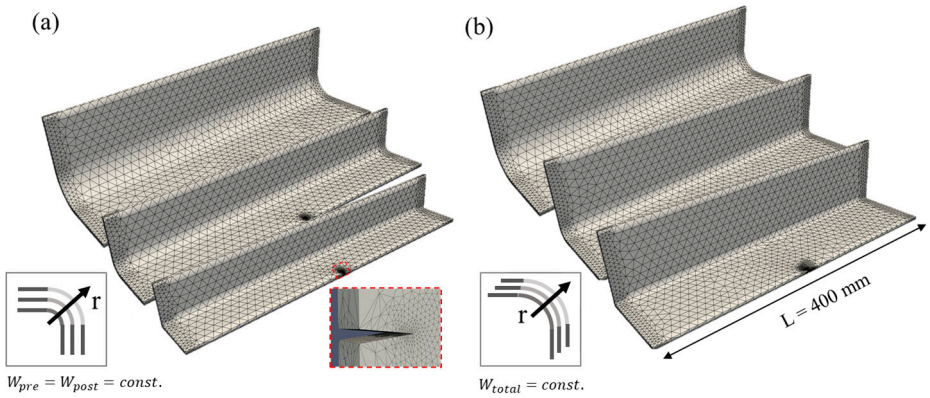


**Figure 2.** Exemplary meshed geometries for special case of α = 90°. (**a**) Variant V1_WPREPOST from r = 0 mm (front) with detailed view on artificial crack to r = 50 mm (back). (**b**) Variant V2_WTOTAL from r = 0 mm (front) to r = 50 mm (back).

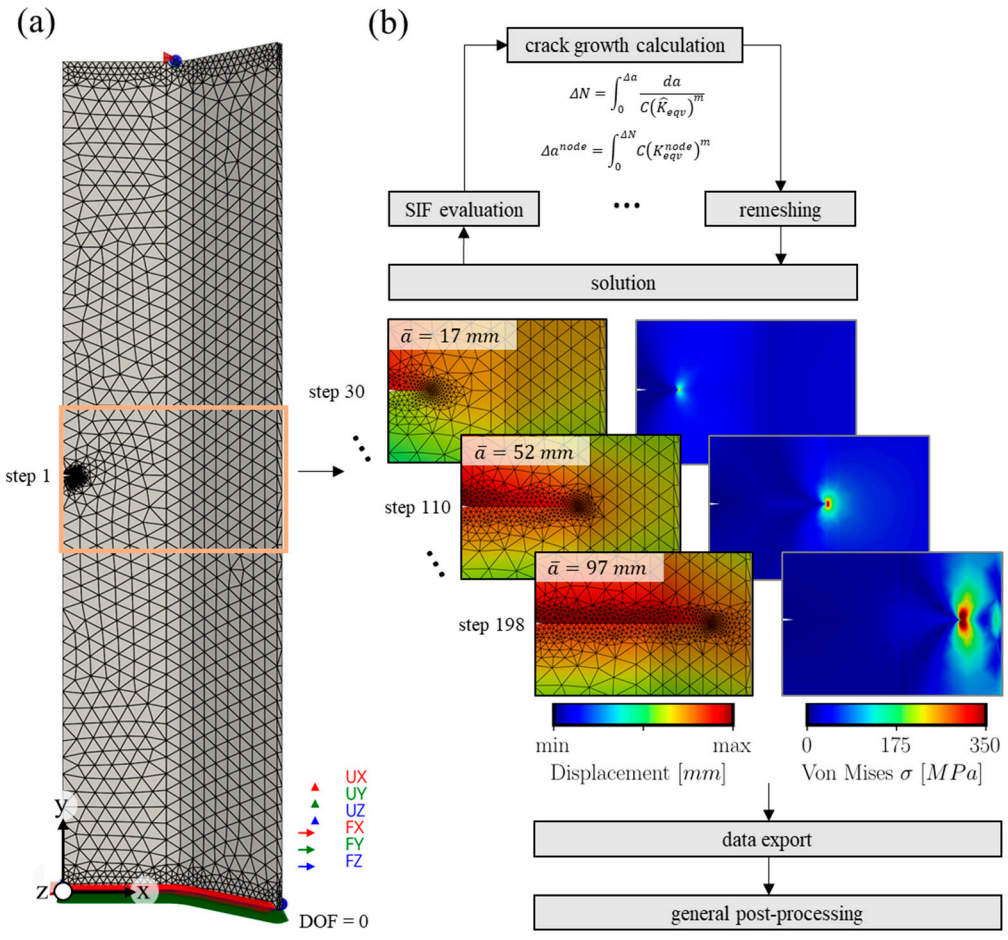


**Figure 3.** Meshed model and solution process. (**a**) Initial mesh for t = 4 mm; α = 40°; and r = 20 mm. (**b**) Schematic workflow. The model section shown is limited to the area of interest around the crack path subject to adaptive remeshing during solving.

The force, $F_y = \sigma_0 A_{Base}$, at the remote point S (APDL Command: F,S,FY,Fy) was calculated by the constant nominal remote stress ($\sigma_0 = 25$ MPa), and the base area, $A_{Base}$,

was defined through the geometry parameters. Except for UY, all other DOFs (translations, rotations) were suppressed. The constant amplitude load was applied as a one-step function (APDL command: KBC,OFF) with $F_{max} = F_y$ and $F_{min} = 0$. It is worth mentioning that the analysis inherently allowed for crack-face closure (or, to be more precise, intersection). In principle, a negative SIF resulting from intersecting crack-front regions would lead to partial crack-front arrest (see Equations (3) and (4)) in the respective subsection. However, negative SIFs were not observed in the simulations. Achieving such negative SIFs would necessitate strong bending moments relative to the axial load on the crack front, which were effectively restricted by the rotational constraints imposed at the remote point.

Sobotka and McClung [42] showed for the out-of-corner parts of a C-section that the SIF can be significantly higher than that of a straight sheet under identical loading conditions. As for the reference, for each $W_{total}$ observed, a "straightened" model was derived accordingly.

The curved sheet models were meshed with higher-order, 3D, 10-node SOLID187 tetrahedron elements with a quadradic displacement formulation. In general, those elements are well suited for modeling irregular meshes and are also required by the SMART algorithm. Figure 3a shows the mesh for the geometry presented in Figure 1d. The mesh could be portioned into three parts: the global mesh, a refined mesh at the boundaries and the refined part around the crack front.

The global mesh size was set to $Esize_{global}$ of 2·t (APDL Command: ESIZE,ALL, $Esize_{global}$). The mesh size appears relatively large, but it should be noted that the material's definition is linearly elastic and the focus was on the contours close to the crack tip. Sensitivity studies of mesh size showed that a more refined mesh in the regions outside the remeshing zone had a negligible influence on the calculated SIF. The mesh around at boundaries was further refined (APDL command: NREFINE,ALL,1,1) which showed increased numerical stability. To avoid remeshing errors at the start of the simulation, the region around the notch was also initially refined to match the crack-front element size, $Esize_{cf}$, of t/8 (APDL command: RMCONT, ESIZ, $Esize_{cf}$). The crack-front elements were equally distributed along the crack front. As a result, the crack front was formed from a total of 21 nodes (11 corner, 10 mid-side).

The SMART tool (APDL Command: CGROW,METHOD,SMART) offered in-solver adaptive remeshing after each solution step for crack advancement. The position of the new crack-front nodes was determined by the fracture parameters of the previous crack-front node component. Alshoaibi [47] showed this method's excellent agreement with formerly reported experimental and numerical methods for crack growth under mixed-mode loading. Figure 3b shows the iterative process of crack growth and adaptive remeshing as well as the formation of the characteristic butterfly-shaped crack tip stress field. The evaluation by the well-known interaction integral method [48–51] (APDL command: CINT,TYPE,SIFS) in its 3D implementation was chosen as the basis for the SIF evaluation. The out-of-plane crack growth direction was based on the Erdogan and Sih proposed maximum circumferential stress criterion [52] via the following:

$$\theta = cos^{-1}\left(\frac{3\hat{K}_{II}^2 + \hat{K}_I\sqrt{\hat{K}_I^2 + 8\hat{K}_{II}^2}}{\hat{K}_I^2 + 9\hat{K}_{II}^2}\right) \quad (1)$$

$$\Delta\hat{K}_{eqv} = \frac{1}{2}cos\left(\frac{\theta}{2}\right)\left[\left(\Delta\hat{K}_I(1 + cos(\theta)) - 3\Delta\hat{K}_{II}^2 sin(\theta)\right]\right. \quad (2)$$

where $\hat{K}_I$ and $\hat{K}_{II}$ are the respective maximum SIFs along the crack front and $\theta$ is the crack deflection angle as a variable for weighting the components. $K_{III}$ is a crack-deflecting quantity and was not implemented in the used version and therefore not considered. To account for this limitation, the chosen boundary conditions ensured that the tearing mode was effectively suppressed. The in-plane crack growth direction was evaluated for each crack-front node. The underlying fatigue crack growth law was defined according to the

Paris equation, $da/dN = C(\Delta K_{eqv})^m$. $\hat{K}_{eqv}$ considered mixed mode but collapsed to $K_I$ for pure Mode-I loading, such as when $\theta$ became 0°, respectively. $\Delta K_I$ became $K_I$ for the stress ratio R = $K_{min}/K_{max}$ = 0. Table 2 lists the crack growth parameters $C$ and $m$ as well as the remaining required material parameters, namely Young's modulus, E, and Poisson's ratio, $v$. The values were in the range of typical high-strength aluminum alloys, e.g., the 7000 and 2000 series [25,53,54] commonly used in critical aerospace applications [55,56]. By assuming a bending process, the crack growth behavior in both legs was implicitly approximated to be governed by the same material law in contrast (e.g., a milling process) as the microstructural orientation in relation to the nominal crack growth direction did not change when the sheet was reshaped. The material behavior was defined as linear–elastic and isotropic. The model was in its initial stress-free state. The formulation was sufficient to account for purely geometric effects. As a remark, material models with plasticity and anisotropy formulation were presently not implemented for SMART.

**Table 2.** High-strength aluminum material and crack growth parameters. Unit system: da/dN : $[\mathrm{mm/cycle}]$; $\mathrm{K_I}$ : $[\mathrm{MPa}\sqrt{\mathrm{m}}]$.

| Material | Symbol | Value |
|---|---|---|
| Young's modulus | E | 71 GPa |
| Poisson ratio | v | 0.33 |
| Stress ratio | R | 0 |
| Paris–Erdogan coefficient | C | $2.25 \times 10^{-7}$ |
| Paris–Erdogan exponent | m | 2.5 |

To calculate the crack growth increments, the life cycle method (APDL Command: CGROW,FCG,METH,LC) was chosen, suitable for constant amplitudes. Here, the number of virtual load cycles $\Delta N$ was a function of the virtual crack growth increment $\Delta a$ and the maximum SIF $\hat{K}_{eqv}$ along the crack-front:

$$\Delta N = \int_0^{\Delta a} \frac{da}{C(\hat{K}_{eqv})^m} \tag{3}$$

where $\Delta a = \tau Esize_{cf}$ and $\tau$ is a multiplication factor between 0.5 and 2. The offset of the new crack-front nodes $\Delta a^{node}$ (with special cases $\Delta a^{ins}$ and $\Delta a^{out}$) was then evaluated node by node for the calculated $\Delta N$:

$$\Delta a^{node} = \int_0^{\Delta N} C\left(K_{eqv}^{node}\right)^m \tag{4}$$

A total of 6 contours around the crack front (APDL command: CINT,NCON,6) were evaluated, while the crack growth itself was driven by $\mathrm{K_I}$ in the second contour (APDL command: CGROW,FCOPTION,MTAB,1,2). This approach balanced the fast convergence observed for contours greater than 1 with the risk of contours further from the crack tip extending beyond the models' boundaries. Other command specifications for the fatigue crack growth (APDL command: CGROW,FCG,Par1,Par2) were set to default values. To avoid remeshing errors, each simulation terminated at a crack length of $\mathrm{W} - \mathrm{W_{post}}/2$.

For a typical model with $\mathrm{W_{total}} = 200$ mm and t = 4 mm, we started with about 34k elements and 56k nodes. If we let the crack grow for 290 substeps, we ended up with about 69k elements and 91k nodes in the final substep. This resulted in a comparatively low computational load throughout the analysis, yet we were able to derive meaningful values as we could always guarantee a suitable and fine mesh around the crack front. This underlined the advantages of the approach chosen.

It is worth mentioning that the linear–elastic material model inherently limited the ability to capture (plasticity-induced) crack closure phenomena, which is indeed relevant for determining absolute service life values for real-world components. While it was possible to incorporate crack closure effects into the analysis (see Equations (2)–(4)) by

calculating an effective stress intensity factor range ($\Delta K_{eff}$) as a function of the stress ratio (R) following established approaches by Elber, Schijve, Newman and others, the primary objective of this work was to compare the influence of geometry parameters on crack growth. The effective stress intensity factor could be expressed as $\Delta K_{eff} = U \cdot \Delta K_{eqv}$, where $U = f(R)$ is the correction factor, and the corresponding crack growth rate was determined as $da/dN = g(\Delta K_{eff})$. Therefore, without the inclusion of non-proportional loading or other secondary effects, the inclusion of crack closure in this analysis would result in a proportional scaling of the remaining life cycles in all cases (with U treated as a constant value for R = 0). Such an approach would not alter the comparative trends in the geometry-dependent crack growth behavior, which was the focus of this work. Consequently, crack closure effects were not explicitly modeled, as their inclusion would not provide new insights into the influence of geometry parameters on the fatigue crack growth and SIF under the present assumptions.

## 3. Results

In the following, a selection of representative results is shown before the overall implication of the geometrical variations in the bending angle, the bending radius and the sheet thickness are discussed. When modeling the crack growth in complex geometries, the path and shape of the traversing crack front were not readily apparent. This complexity required a detailed analysis, as outlined in the subsequent section.

### *3.1. Crack Front*

The non-uniformity around the mid-axis of the L-section shape caused a non-uniform stress distribution at the crack front under remote loading due to out-of-plane bending as recognized by Huang et al. [43]. As a result, the traversing crack front might have differed from the symmetric crack-front hypothesis. Figure 4 shows the crack path for two L-shaped geometries with (a) r = 0 mm and (b) r = 10 mm. Crack growth only occurred in the xz-plane. Overall, the out-of-plane deviations of individual nodes introduced by a $K_{II}$ fraction were less than 0.2% and could be attributed to numerical inaccuracies. The letters A, B and C in (a) indicate prominent points, which are marked in Figure 6d for reference.

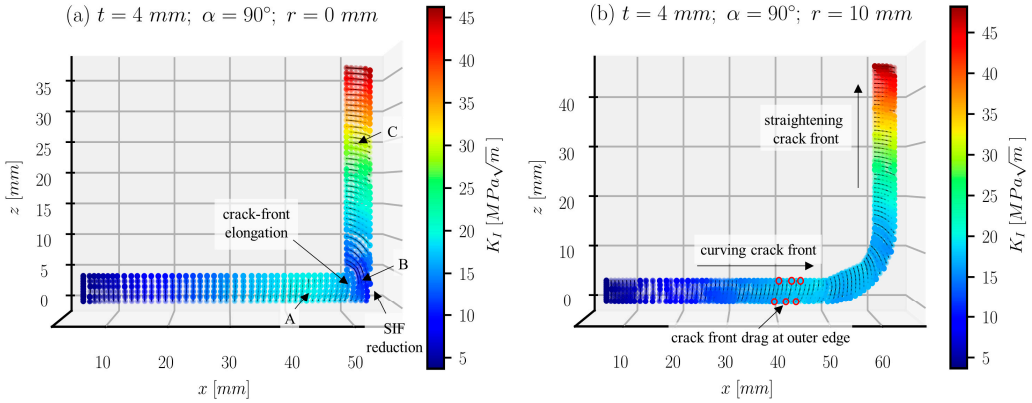


**Figure 4.** Crack-front evolution for two L-shaped geometries sampled from V1_WPREPOST with (**a**) r = 0 mm and (**b**) r = 10°mm. The letters A, B and C indicate prominent points, which are marked in Figure 6d for reference. Markers indicate crack-front corner nodes. Black lines between the markers indicate the calculated crack-front geometry of each separate load step.

For all geometrical variations, the crack started at x = $a_{pre}$ = 5 mm. As expected from the loading conditions and the shape of the notch, the initial crack front was straight for the first few iterations, as indicated by the connected dots, representing the corner nodes of the elements. After the crack growth furthered, several effects could be observed. The first observation was the increasing elongation of the crack front as it moved towards the corner region. This is particularly evident in (a), where it shows that the crack-front length reached

a maximum of 8.6 mm, which was more than two times the sample thickness. However, this effect also occurred before the transition in the corner region, which can be seen more clearly in (b). It was more pronounced in the pre-corner region for samples with a bigger bending radius (b) in contrast to the less-pronounced overall elongation of 5.3 mm. When the corner region was passed, the crack-front length converged towards t and, meanwhile, the free boundary node drag decreased. The elongation was accompanied by a mismatch of the x- and z-positions, respectively, of the two nodes on the opposing free surfaces.

These individual results already show that the developing crack-front geometry in the angle profiles deviated from that of a flat plate under given boundary conditions and that this deviation was not strictly limited to the corner region. This implies that the longitudinal shear forces and the additional out-of-plane bending moment [43] present in this integral configuration under remote loading incrementally altered the crack-front shape in response.

Figure 5 shows the maximum of the thickness-normalized crack-front width $c_{cf}/t$ for the three thicknesses studied as a function of r and $\alpha$. As illustrated in Figure 4, the maximum elongation consistently occurred in the corner region. For the full parameter set (here, V1_WPrePost), it is clearly evident that, independent of t, the crack-front elongation was most pronounced for small radii and quickly approached unity with an increasing radius. An inverse trend occurred for $\alpha$, where the maximum crack-front width increased with the bending angle. Peaking at the discontinuity (r = 0 mm) and $\alpha$ = 120 °, the $c_{cf}$ reached up to 2.5 times the sheet thickness in the corner region. Furthermore, it is clearly visible that in the corner region the in the sample's surface's observable crack front, spanned by the points of intersection on the inner and outer surfaces (see also $c^{ins,out}$ as their magnitude), the crack-front was not parallel to the respective surface normal. Here, the crack front was shaped similarly to an ellipsoidal corner crack. There was a non-negligible mismatch in the crack length between the length measured along the geometry's neutral fibre and the crack length given by the accumulated crack-front increments $\Delta a^{ins}$ and $\Delta a^{out}$, respectively.

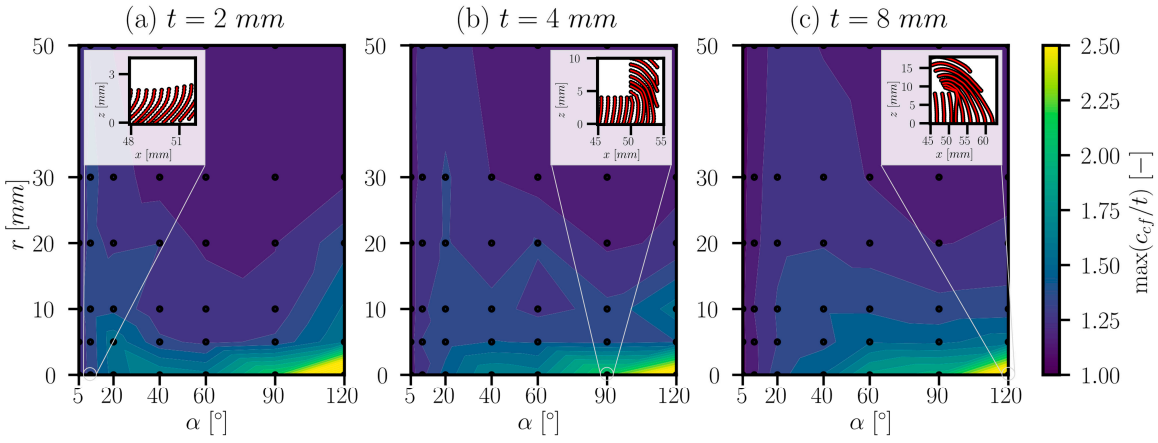


**Figure 5.** Maximum deviation occurring from straight crack-front geometry in parameter study (V1_WPrePost) indicated by normalized crack-front parameter for (**a**) t = 2 mm; (**b**) t = 4 mm; and (**c**) t = 8 mm.

Therefore, the mean crack length $\bar{a} = \sum_{i=1}^{n} \Delta a_i^{node}/n$ as the mean value over all crack-front nodes, with n as the number of the current substep, was introduced as the reference value.

In this modeling approach, the crack growth and therefore the crack-front geometry was governed by the distribution of the SIF (Equation (4)) along the crack front and the maximum SIF (Equation (3)) as well. Consequently, the following subsection will focus on the analysis of the SIF evolution in an angled sheet.

### *3.2. Sheet Geometry and Stress Intensity Factors*

In accordance with the Griffith crack, $K_I = \sigma_0\sqrt{\pi a}$, as the basis for linear–elastic fracture mechanics, the SIF tended to increase with an increasing crack length. However, as already shown for the case presented, this increase was not monotonic. It was noticeable that the SIF evolution showed a local minimum (or minima) in the corner region, as seen in Figure 4. The crack-front elongation coincided with these minima. This effect was more pronounced for r = 0 mm, where the local minimum for the given example was located at the mean, $\overline{K}_I = 11\ \mathrm{MPa}\sqrt{m}$, and $\bar{a} = 52$ mm. The geometric reduction in the SIF was equivalent to a reduction in the crack length by 54% by that point. For r = 10 mm, the local minimum was located at the mean, $\overline{K}_I = 16\ \mathrm{MPa}\sqrt{m}$, and $\bar{a} = 56$ mm, which still corresponded to a reduction of only 37%.

There was also an SIF gradient over the crack-front length when it was measured as $\bar{a}$, as previously described. Overall, the mean deviation between the minimum and maximum SIF along the crack-front solution step was 4.5% for a given $\bar{a}$. For the studied parameter sets, the maximum deviation (outside and inside nodes) was up to 30% for elongated crack fronts like those shown in Figure 5c yet outweighed by the overall trend of a decreasing SIF in the corner region. This effect was a result of discretization of the crack growth increments. Hence, with smaller crack growth increments and element sizes, the deviation could be further lowered at the expense of computational resources. This result demonstrated that the parameterization of the crack front was non-trivial when there were substantial discontinuities in the geometry.

In the case presented, the service life was measured in loading cycles, N, as a function of $f(\hat{K})$ of the maximum SIF along the crack front. Based on the results, it can be argued that the mean value would not be more appropriate for consideration in regard to a straightened sheet, because the difference in the SIF along the crack front observed for straight crack fronts was already dissipated by its reshaping effect. Since it also equalized over numerical uncertainties, the latter approach was taken and would therefore continue to use the mean SIF, $\overline{K}$, as function of $\bar{a}$ as the basis for further calculations in the post-processing of the results if not stated otherwise.

To further investigate the individual contribution of the geometry parameters to the SIF, several variations in the (a) bending angle, $\alpha$, (b) bending radius, r, and (c) thickness, t, are comparatively contrasted in Figure 6. From the individual graphs, it is evident that all geometrical variations influenced the evolution of the SIF. The variation in $\alpha$ in (a) for a sheet with t = 4 mm and r = 30 mm shows in the corner region (indicated by the dotted lines) a more distinctive drop in the SIF with an increasing $\alpha$. The overall shape of the curve also changes. While the curves for $\alpha = 10°$ and $\alpha = 60°$ show a single local minimum located in the crack length increment attributed to the corner region, at the maximum angle of 120°, the graph displays two minima here. The SIF curve is therefore not simply stretched in (a) as might be suggested by the increase in the total crack length due to the increased sample length for V1_WPrePost. The variation in r in (b), on the other hand, shows a curve similar to a stretch in the corner region. The stronger deviation compared to (a) in the lower K region between 10 and 20 $\mathrm{MPa}\sqrt{m}$ in front of the corner region ($\bar{\mathbf{a}}$ between 25 and 50 mm) is particularly noticeable. Here, K (and so $\Delta K$ for given R) tends to be lower for a greater r. This contrasts with the lower minimum of K with a lower r in the corner region. Derived from the exponential relationship between the SIF and the crack growth rate (da/dN), the low $\Delta K$ range is particularly decisive for the total service life under fatigue loads. For the variation in t shown in (c), the influence is similar to that of $\alpha$, whereby for lower thicknesses the shape of the curve also assumes an approximately bicubic shape in the corner region. Overall, this must be offset against the total length increase as W = f(r) for V1_WPrePost (and, therefore, increased nominal lifetime) and is considered again separately for the model variation V2_WTotal and V3_BBox, presented in (d) as subset of V1_WPrePost compared to (e) and (f).

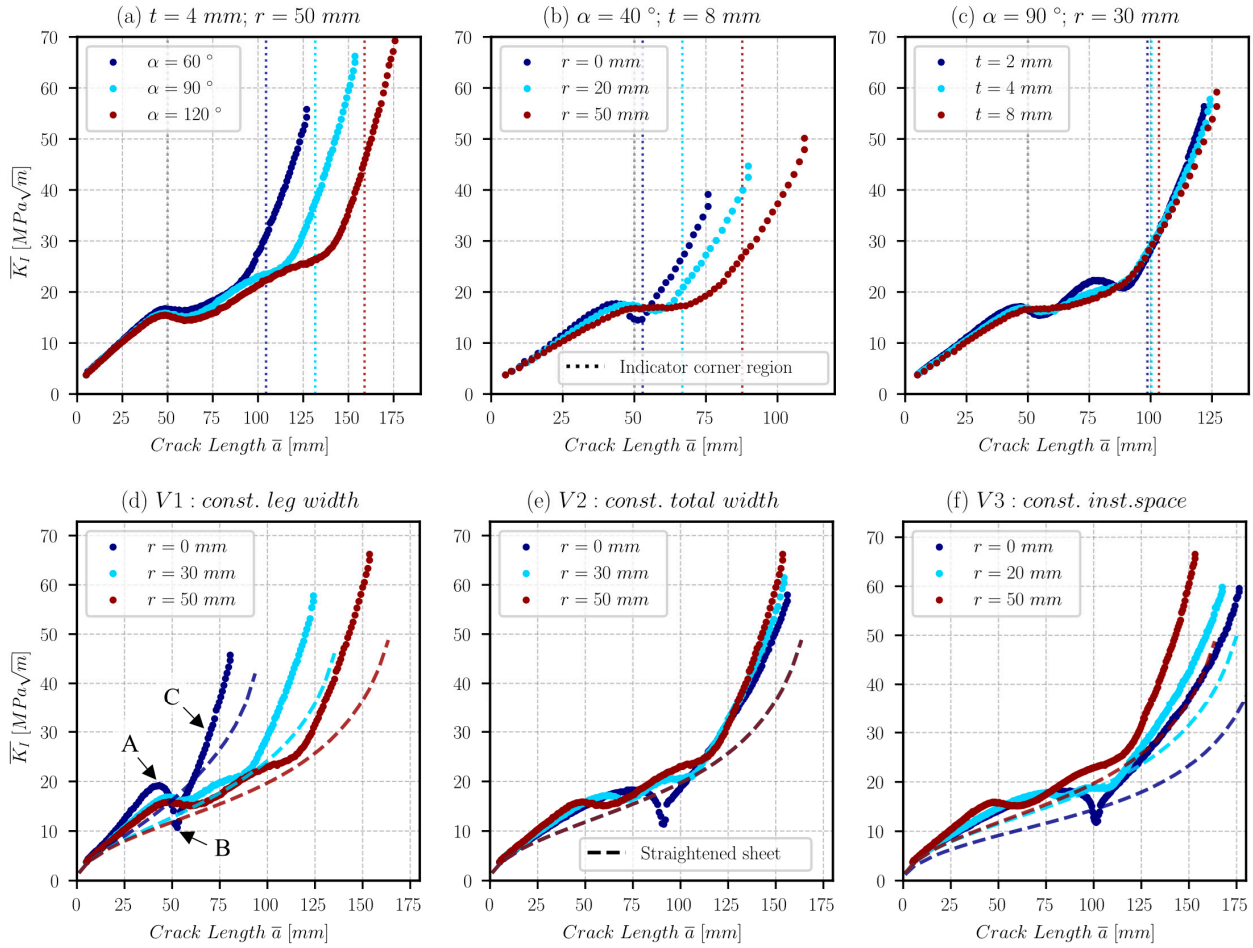


**Figure 6.** An exemplary SIF KI over the crack length, a, for the model variant V1_WPrePost. (**a**) The bending angle, (**b**) bending radius and (**c**) sheet thickness are comparatively contrasted. Dotted lines mark the crack length increment assigned to the corner region. (**d**–**f**) show exemplary curves for t = 4 mm and α = 90° and V1_WPrePost to V3_BBox, respectively. The letters A, B and C indicate prominent points, which are marked in Figure 4a for reference. Dashed lines indicate the SIF for straightened sheets of equivalent widths as a reference.

The SIF curves are sampled from the lowest to the highest r and with a constant t = 4 mm and α = 90°. In addition, the straightened sheet solution as reference is provided. The letters A, B and C in (d) indicate prominent points, which are marked in Figure 4a as a reference for the crack length, $\overline{\mathbf{a}}$.

As can be observed here, for the given set of boundary conditions, the crack tip load is greater than that of a straight sheet of an equivalent length, with the exception of a few sections that depend on the parameter r. For smaller radii (r), the effect is more pronounced and also dependent on other geometry parameters; in the case of V2_WTotal and V3_BBox, it depends on the derived leg lengths.

From the exemplary observations, it is evident that all three geometrical parameters examined in this study influenced the SIF along the crack front when the crack was growing through the component. In all cases examined, an arc in the sheet led to local minima in the SIF in the corner region. When the crack grew through that segment, the SIF monotonically increased in accordance with the Griffith crack. This late stage was governed by the ratio $\overline{\mathbf{a}}/W_{total}$ (hence, r and α for V1_WPREPOST) and not by t.

## 4. Discussion

In the following, the focus is on sheet thickness of t = 4 mm as this study did not observe any unique sheet thickness effects. Qualitatively, the observed effects in the corner region occurred in all thickness variations, albeit with varying magnitudes for the values of r and $\alpha$.

For the following discussion, the single-edge crack solution for a finite plate with one end fixed and the opposite end under remote tension was derived. In practice, such an approximate solution could be used as a first step in the design process but may not be sufficient for component testing. Sobotka and McClung [42] showed for the out-of-corner parts of a geometrically similar C-section under different loading and boundary conditions that an approximation could only be readily made under fully constrained boundary conditions. They showed that for the unrestricted (no restrictions on the cross-section deformation)-to-intermediate state, the SIF for a crack in the first flange and in the web of a C-section could be several times higher than the SIF of a crack of equal length in the straightened sheet. Similar behaviour could be expected for the L-Sections of this study.

Finally, we derive the expected service lifetimes for V1_WPrePost, V2_WTotal and V3_BBox for a design-relevant subset and discuss the results of this study in terms of their implications for real-world components.

### *4.1. Normalized Stress Intensity Factors and Sheet Sections*

In Figure 7, the normalized mean SIF as the ratio, $\overline{K_I^A}/\overline{K_I^S}$, of the SIF of an angled sheet, $\overline{K_I^A}$, to the SIF of straightened sheet of an equivalent width, $\overline{K_I^S}$, for two exemplary sets of geometry parameters for the model variation V1_WPrePost are presented. Since the sheets were of different lengths because of the geometrical variations in the corner region, the crack length was normalized by the length of the maximum possible crack lengths, $\left(l_{pre} = W_{pre}, l_{corner} = f(\alpha, r, t), l_{post} = W_{post}\right)$, in each section to account for the total lifetime of the component. Figure 7a shows the exemplary case for an L-section with $\alpha$ = 90° and t = 4 mm for root radii (r) from 0 to 50 mm. For small crack lengths, $a \rightarrow a_{pre} = 5$ mm, the solutions for the L-section and equivalent straightened sheet were of equal value, $\left(\frac{\overline{K_I^A}}{\overline{K_I^S}} \rightarrow 1\right)$. With increasing a in the pre-corner section, however, $\overline{K_I^A}$ initially increased relative to $\overline{K_I^S}$ to a maximum of about 1.4 for r = 0 mm and 1.35 for r = 50 mm. The variation was considerably small, but by the exponential relationship between $\Delta K$ and the crack growth rate (da/dN), the fatigue life prediction was especially sensitive to variations in the low $\Delta K$ regime. The intermediate radii were between these values but converged to the curve of r= 50 mm up to their maximum. The shape of the family of curves was concave with an intersection point at $\left(\frac{\bar{a}}{l_{pre}}, \frac{\overline{K_I^A}}{\overline{K_I^S}}\right) = (0.82, 1.35)$. From here (and prior to the geometrically defined intersection), $\overline{K_I^A}$ dropped sharply with a gradient inversely proportional to the radius, indicating a possible retarding effect on the crack growth rate compared to a straight plate. In the case of r = 0 mm, it dropped below $\overline{K_I^S}$ to $\frac{\overline{K_I^A}}{\overline{K_I^S}} = 0.86$ at $a = l_{pre}$.

In the corner region, the relationship is more complicated, as already indicated by the absolute $\overline{K_I^A}$ curves in Figure 6. For the smaller root radii (r = [0;5;10] mm), there is a retardational effect induced by the intersectional area resulting in $\overline{K_I^A} < \overline{K_I^S}$ in most of the corner region with a minimum of $\frac{\overline{K_I^A}}{\overline{K_I^S}} = 0.57$ for r = 0 mm. The effect decreases with higher radii; for r > 30 mm, $\overline{K_I^A} > \overline{K_I^S}$ in the full corner region. An increase in r simultaneously leads to increased symmetry in the curves in the corner region, resulting in an approximately symmetric curve of an even, biquadratic shape for r = 50 mm and one that is axisymmetric about the centre of the corner region. This is geometrically accompanied

by an intermediate straightening of the crack front which then leads to a second minimum when the crack grows further.

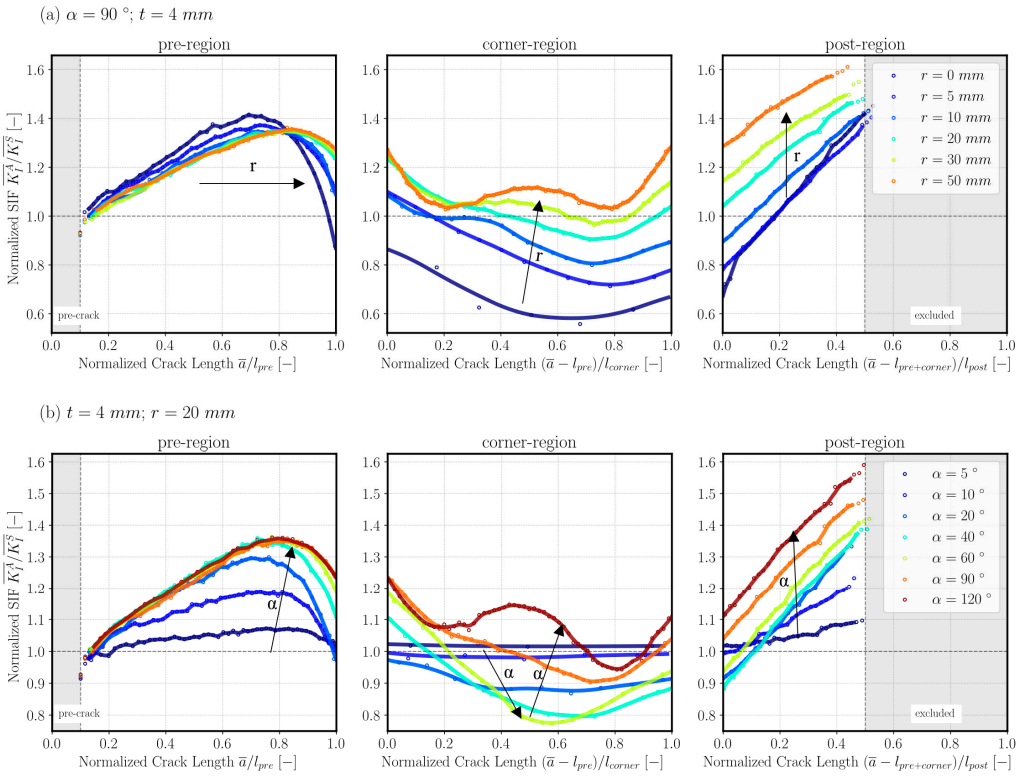


**Figure 7.** Normalized stress intensity factors for the crack length, a, for the model variant V1_WPrePost. Variation in the (**a**) bending radius and (**b**) bending angle. The normalization was carried out against the stress intensity factors ($K_I^S$) solution of a straight sheet of the same total width, W.

In the post-corner region, the relationship between r and $\frac{\overline{K_I^A}}{K_I^S}$ is proportional. The ratio $\frac{\overline{K_I^A}}{K_I^S}$ monotonically increases with the crack length but the gradient is approximately invariant with respect to r. The curves are shifted by an offset of approximately 0.1 to each other. For r = 0 mm, the curve deviates from the general trend. This can be attributed to numerical inaccuracy, evident from the abrupt increase in $\overline{K_I^A}$ when the crack exits the corner region. The results suggest that the approximation of an L-profile by a straightened sheet of equal length would underestimate the SIF in the pre-region and therefore overestimate the service life increment attributable to this segment and subsequently the total lifetime of the component due to the exponential relationship between the crack growth rate and ΔK given by the Paris law.

Figure 7b explores the case for a constant t = 4 mm and r = 20 mm and a variable bending angle α from 5° to 120°. The 0° variant (straightened sheet) is again represented by the $\frac{\overline{K_I^A}}{K_I^S} = 1$ horizontal line. In general, for small alphas $\frac{\overline{K_I^A}}{K_I^S} \to 1$, the SIF hence approaches that of a straightened sheet, which is expected from plate theory. However, the curve already deviates upwards by up to 20% for α = 10° in the pre-region for short a $a/l_{pre} < 0.8$. This behaviour exhibits a further increase with an increasing α but converges to the limit value $\frac{\overline{K_I^A}}{K_I^S} \to 1.35$ for α > 60°. Similarly to the case of the variable r, the shape of the curve is concave over the entire α range considered in this study. Overall, the curves converge for α ≥ 60° to a constant $\frac{\overline{K_I^A}}{K_I^S}$ for a given $a_{pre}/l_{pre}$. This behaviour for α ≥ 60°

persists up to $\frac{(a-l_{pre})}{l_{corner}} \approx 0.18$ in the corner region. In the corner region, the behaviour is more complex. For $\alpha \leq 10°$, the arc is sufficiently well approximated by the straightened sheet and $\frac{\overline{K_I^A}}{\overline{K_I^S}} \to 1$. This is contrary to the evolution of o$\frac{\overline{K_I^A}}{\overline{K_I^S}}$ in the pre-section, where max$\frac{\overline{K_I^A}}{\overline{K_I^S}} \approx 1.2$ for $\alpha = 10°$. It can also be observed that the mean $\frac{\overline{K_I^A}}{\overline{K_I^S}}$ in the corner section does not monotonically increase with $\alpha$ up to a convergence value but decreases from $\alpha = 5°$ to $\alpha = 40°$ and then increases again for $\alpha > 40°$. The maximum explored angle $\alpha = 120°$ exhibits an approximately biquadratic shape.

In the post-corner region, the ratio $\frac{\overline{K_I^A}}{\overline{K_I^S}}$ monotonically increases with the crack length. For $\alpha = 5°$ to $\alpha = 20°$, the gradient increases as well, while for $\alpha > 20°$, the gradient is constant, and for the greater bending angles, there is also a more distinctive offset.

The results for both examples in Figure 7a,b indicate that for partially constrained L-sections with axial loading, a straight sheet approximation might be not sufficient to describe the fatigue lifetime of the component. As pointed out by other authors [43–45,57], when the crack approaches and grows into the stiffener (or the second leg for the geometry presented in this work), the effective load on the crack front decreases. The relationship becomes increasingly complex for the end points of r and $\alpha$ in the parameter space. In contrast to the middle crack loaded under uniform tension, presented in the aforementioned publications, the edge crack under axial loading might grow faster than in an unstiffened, flat plate. Especially for shorter crack lengths, such as in the pre-corner region, the SIF exceeds that for an equivalent straightened sheet, even if this section itself is not curved.

### *4.2. Estimated Fatigue Life*

Estimating the remaining service lifetime of a component is crucial for ensuring its reliability and safety, especially in applications subjected to fatigue loading. This study has highlighted the significant influence of geometric parameters such as the sheet thickness, bending angle and bending radius on fatigue cracks' growth behaviour. Among these, the bending radius is particularly relevant from a production perspective, as it affects both the mechanical properties and manufacturability of the component for the given process. It should be noted, even though they were not explicitly considered in this study, that smaller radii might lead to higher localized stresses, accelerating crack initiation and thereby reducing fatigue life. Conversely, larger radii distribute stresses more evenly, delaying crack initiation and slowing crack growth, thus enhancing fatigue life. Additionally, the bending radius impacts manufacturing feasibility with minimal bending radius requirements dictated by material properties and process capabilities. Optimizing the bending radius is essential for improving mechanical performance and extending the service lifetime of components, ensuring greater structural integrity and reliability in practical applications.

In the following, the influence of this geometric size for different variations is discussed. Figure 8 shows the crack length a over the accumulated cycles estimated by Equation (3).

Figure 8a shows V1_WPrePost, the case for constant leg widths. Thus, $W_{total} = f(\alpha, r)$ and $W_{total} \propto \alpha, r$. The estimated remaining lifespan, regardless of the stronger retarding effect for small r (see marked angle region), is dominated by the total width of the sheet. As a result, a wider sheet exhibits more damage-tolerant behaviour throughout the entire crack propagation process.

Figure 8b shows the case for V2_WTotal, i.e., sheets with a constant $W_{total}$ and $W_{pre} = W_{post} = f(\alpha, r)$. The profile is point-symmetric to the radius. As expected by the total SIF values, the expected lifetime for the L-shaped component compared to its straightened variant visibly decreases. At a = 140 mm, N for r = 0 mm is 22% smaller and N for r = 50 mm is 31% smaller than that of the flat plate's equivalent. Even though the arc introduces a minimum SIF for a smaller r lower than that of the corresponding straight sheet's solution, the effect does not outweigh the overall increases in the SIF, especially for

a small a and a corresponding small $K_I$ in relation to it. When comparing the influence of r on N, the influence of the corner region does not alter the general trend with respect to N that is established in the first crack growth increments. When taking a = 140 mm as a critical crack length with $N = N_{total}$, the contribution of the corner region to $N_{total}$ for r = 50 mm is 17%, with diminishing influence for smaller radii (for r < 30 less than 10%).

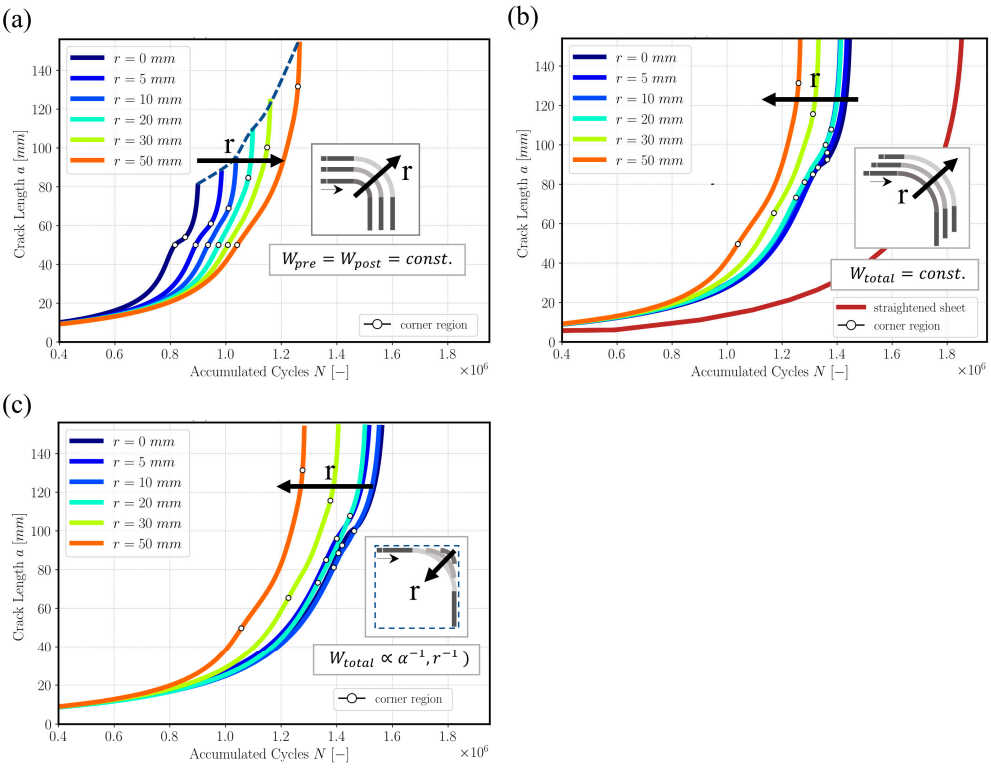


**Figure 8.** Effect of bending radius on residual lifecycles for models (**a**) V1_WPrePost, (**b**) V2_WTotal and (**c**) V3_BBox with α = 90° and σ_0 = 25 MPa. White dots highlight accumulated cycles in corner region.

Figure 8c shows V3_BBox, the consideration for a constant assumed square installation space. Here, the geometry $W_{total} = f(\alpha, r)$ is the same as for the case of a constant leg width, $W_{total} \propto \alpha^{-1}, r^{-1}$. A smaller bending radius allows for a better approximation of the installation space contour and thus an overall higher sheet width for small radii. This effect adds to the previously presented higher lifespan with a decreasing bending radius in the case of (b).

Therefore, exact modeling in the pre-corner region is most important for fatigue lifetime prediction under crack growth. For the estimated fatigue life with the isotropic, Paris–Erdogan material model, greater bending radii are less beneficial for an L-shaped component than smaller ones.

## 5. Conclusions

The three-dimensional finite-element crack growth analysis conducted in this study provides valuable insights into the geometric factors influencing fatigue crack growth in angled sheets under axial loading. The findings can be summarized as follows:

- Negligible effect of sheet thickness on SIF outside radius: this study revealed that variations in the sheet thickness had a minimal impact on the SIFs outside the bending radius region.
- Bending angle and radius were highly relevant: both the bending angle and bending radius significantly influenced the SIFs and crack growth behaviour.

- Remaining service life of L-type profile less than straight plate: the curved L-shaped plates exhibited a shorter fatigue life compared to the straight plates due to increased crack-front loads at small crack lengths starting from one of the legs.

Increasing radius reduced damage tolerance under pure external axial loading: increasing the root radius was found to reduce the fatigue life because of the higher overall SIF found for crack lengths spawning in the pre-corner region.

The current analysis, based on a linear–elastic solution, provides valuable insights. It simplifies the complex real-world behaviour of L-shaped components under fatigue loading. It was shown that both the shape and orientation of the crack front were not easily parameterizable, and the crack-front orientation in the crack plane as a function of the mean crack length or the crack length measured along the neutral fiber presented further complexities.

**Author Contributions:** Conceptualization, F.D., F.P. and E.B.; methodology, F.D. and F.P.; software, F.D.; validation, F.D.; formal analysis, F.D.; investigation, F.D.; resources, F.D.; data curation, F.D.; writing—original draft preparation, F.D.; writing—review and editing, F.D., F.P. and E.B.; visualization, F.D.; supervision, E.B.; project administration, E.B.; funding acquisition, E.B. All authors have read and agreed to the published version of the manuscript.

**Funding:** This research was funded by the German Federal Ministry for Economic Affairs and Energy (BMWi) through the project GRETA embedded in the German aeronautic research fund LuFo 2020-2024 (code 20W1904G).

**Data Availability Statement:** The authors declare that the data supporting the findings of this study are available within the article and its supplementary information files are published on Zenodo. The code is available on our github repository: https://github.com/dlr-wf/ANSYS-SMART-angled-sheet-sections, (accessed on 21 November 2024).

**Conflicts of Interest:** The authors declare no conflicts of interest.

## References

1. Findlay, S.; Harrison, N. Why aircraft fail. *Mater. Today* **2002**, *5*, 18–25. [CrossRef]
2. Afonso, F.; Sohst, M.; Diogo, C.M.; Rodrigues, S.S.; Ferreira, A.; Ribeiro, I.; Marques, R.; Rego, F.F.; Sohouli, A.; Portugal-Pereira, J.; et al. Strategies towards a more sustainable aviation: A systematic review. *Prog. Aerosp. Sci.* **2023**, *137*, 100878. [CrossRef]
3. Kaspar, J.; Vielhaber, M. Sustainable Lightweight Design—Relevance and Impact on the Product Development & Lifecycle Process. *Procedia Manuf.* **2017**, *8*, 409–416. [CrossRef]
4. Ingarao, G.; Zaheer, O.; Fratini, L. Manufacturing processes as material and energy efficiency strategies enablers: The case of Single Point Incremental Forming to reshape end-of-life metal components. *CIRP J. Manuf. Sci. Technol.* **2021**, *32*, 145–153. [CrossRef]
5. Lihui, L.; Kangning, L.; Cai, G.; Yang, X.; Guo, C.; Bu, G. A critical review on special forming processes and associated research for lightweight components based on sheet and tube materials. *Manuf. Rev.* **2014**, *1*, 9. [CrossRef]
6. Madhusudhana, H.K.; Gaitonde, V.N.; Satish Jangali, G. A Review on Lightweight Metal Component Forming and its Application. *J. Phys. Conf. Ser.* **2021**, *2070*, 12246. [CrossRef]
7. Richter, K.; Müller, R.; Kunke, A.; Kräusel, V.; Landgrebe, D. Manufacturing of Long Products Made of Innovative Lightweight Materials. *Acta Metall. Sin. (Engl. Lett.)* **2015**, *28*, 1496–1502. [CrossRef]
8. Schijve, J. Fatigue damage in aircraft structures, not wanted, but tolerated? *Int. J. Fatigue* **2009**, *31*, 998–1011. [CrossRef]
9. Bush, R.W.; Bucci, R.J.; Magnusen, P.E.; Kuhlman, G.W. Fatigue Crack Growth Rate Measurements in Aluminum Alloy Forgings: Effects of Residual Stress and Grain Flow. In *Fracture Mechanics: Twenty-Third Symposium*; Chona, R., Ed.; ASTM International: West Conshohocken, PA, USA, 1993; ISBN 0-8031-1867-8.
10. Gordon, J.V.; Haden, C.V.; Nied, H.F.; Vinci, R.P.; Harlow, D.G. Fatigue crack growth anisotropy, texture and residual stress in austenitic steel made by wire and arc additive manufacturing. *Mater. Sci. Eng. A* **2018**, *724*, 431–438. [CrossRef]
11. Jimenez-Martinez, M. Manufacturing effects on fatigue strength. *Eng. Fail. Anal.* **2020**, *108*, 104339. [CrossRef]
12. Smudde, C.M.; San Marchi, C.C.; Hill, M.R.; Gibeling, J.C. The Influence of Residual Stress on Fatigue Crack Growth Rates in Stainless Steel Processed by Different Additive Manufacturing Methods. *J. Mater. Eng. Perform.* **2024**, *33*, 7703–7713. [CrossRef]
13. de Florio, F. *Airworthiness: An Introduction to Aircraft Certification and Operations*, 3rd ed.; Elsevier Science: St. Louis, MO, USA, 2016; ISBN 9780081009406.
14. Chabod, A.; Baron, N. Digital Twin For Fatigue Analysis. *Fatigue Aircr. Struct.* **2020**, *2020*, 47–56. [CrossRef]
15. Cianetti, F.; Morettini, G.; Palmieri, M.; Zucca, G. Virtual qualification of aircraft parts: Test simulation or acceptable evidence? *Procedia Struct. Integr.* **2019**, *24*, 526–540. [CrossRef]

16. Gomez-Escalonilla, J.; Garijo, D.; Valencia, O.; Rivero, I. Development of Efficient High-Fidelity Solutions for Virtual Fatigue Testing. In *ICAF 2019—Structural Integrity in the Age of Additive Manufacturing*; Niepokolczycki, A., Komorowski, J., Eds.; Springer International Publishing: Cham, Switzerland, 2020; pp. 187–200. ISBN 978-3-030-21502-6.
17. Ostergaard, M.G.; Ibbotson, A.R.; Le Roux, O.; Prior, A.M. Virtual testing of aircraft structures. *CEAS Aeronaut. J.* **2011**, *1*, 83–103. [CrossRef]
18. Ayhan, A.O.; Yaren, M.F. Effects of microstructural through-thickness non-uniformity and crack size on fatigue crack propagation and fracture of rolled Al-7075 alloy. *Fatigue Fract. Eng. Mater. Struct.* **2020**, *43*, 2071–2084. [CrossRef]
19. Kalina, M.; Schöne, V.; Spak, B.; Paysan, F.; Breitbarth, E.; Kästner, M. Fatigue crack growth in anisotropic aluminium sheets—Phase-field modelling and experimental validation. *Int. J. Fatigue* **2023**, *176*, 107874. [CrossRef]
20. Strohmann, T.; Breitbarth, E.; Besel, M.; Zaunschirm, S.; Witulski, T.; Requena, G. Damage Mechanisms and Anisotropy of an AA7010-T7452 Open-Die Forged Alloy: Fatigue Crack Propagation. *Materials* **2022**, *15*, 3771. [CrossRef] [PubMed]
21. Schijve, J. The effect of pre-strain on fatigue crack growth and crack closure. *Eng. Fract. Mech.* **1976**, *8*, 575–581. [CrossRef]
22. Fukui, Y.; Nunomura, S. Effect of Cold Work on Fatigue Crack Propagation Rate Regarding to the Accumulated Plastic Strain Rate. *J. Soc. Mater. Sci.* **1979**, *28*, 491–496. [CrossRef]
23. Al-Rubaie, K.S.; Del Grande, M.A.; Travessa, D.N.; Cardoso, K.R. Effect of pre-strain on the fatigue life of 7050-T7451 aluminium alloy. *Mater. Sci. Eng. A* **2007**, *464*, 141–150. [CrossRef]
24. Froustey, C.; Lataillade, J. Influence of large pre-straining of aluminium alloys on their residual fatigue resistance. *Int. J. Fatigue* **2008**, *30*, 908–916. [CrossRef]
25. Alrubaie, K.; Barroso, E.; Godefroid, L. Fatigue crack growth analysis of pre-strained 7475–T7351 aluminum alloy. *Int. J. Fatigue* **2006**, *28*, 934–942. [CrossRef]
26. Burlat, M.; Julien, D.; Lévesque, M.; Bui-Quoc, T.; Bernard, M. Effect of local cold working on the fatigue life of 7475-T7351 aluminium alloy hole specimens. *Eng. Fract. Mech.* **2008**, *75*, 2042–2061. [CrossRef]
27. Dematos, P.; Mcevily, A.; Moreira, P.; Decastro, P. Analysis of the effect of cold-working of rivet holes on the fatigue life of an aluminum alloy. *Int. J. Fatigue* **2007**, *29*, 575–586. [CrossRef]
28. Luan, S.; Zhang, C.; Zhang, X. Effect of residual stress redistribution on fatigue crack growth pertinent to crack closure and applied load. *Mater. Des.* **2023**, *233*, 112282. [CrossRef]
29. Tekkaya, A.E.; Bouchard, P.-O.; Bruschi, S.; Tasan, C.C. Damage in metal forming. *CIRP Ann.* **2020**, *69*, 600–623. [CrossRef]
30. Hirt, G.; Tekkaya, A.E.; Clausmeyer, T.; Lohmar, J. Potential and status of damage controlled forming processes. *Prod. Eng.* **2020**, *14*, 1–4. [CrossRef]
31. Cameron, B.C.; Tasan, C.C. Towards physical insights on microstructural damage nucleation from data analytics. *Comput. Mater. Sci.* **2022**, *202*, 110627. [CrossRef]
32. Besson, J. Continuum Models of Ductile Fracture: A Review. *Int. J. Damage Mech.* **2010**, *19*, 3–52. [CrossRef]
33. Mokhtarishirazabad, M.; Lopez-Crespo, P.; Moreno, B.; Lopez-Moreno, A.; Zanganeh, M. Optical and analytical investigation of overloads in biaxial fatigue cracks. *Int. J. Fatigue* **2017**, *100*, 583–590. [CrossRef]
34. Vormwald, M.; Hos, Y.; Freire, J.L.; Gonzáles, G.L.; Díaz, J.G. Crack tip displacement fields measured by digital image correlation for evaluating variable mode-mixity during fatigue crack growth. *Int. J. Fatigue* **2018**, *115*, 53–66. [CrossRef]
35. Camacho-Reyes, A.; Vasco-Olmo, J.M.; James, M.N.; Diaz, F.A. Characterization of non-planar crack tip displacement fields using a differential geometry approach in combination with 3D digital image correlation. *Fatigue Fract. Eng. Mater. Struct.* **2022**, *45*, 1521–1536. [CrossRef]
36. Sipos, A.A.; Cao, S. About Measuring the Stress Intensity Factor of Cracks in Curved, Brittle Shells. *Frat. Integrità Strutt.* **2024**, *18*, 1–17. [CrossRef]
37. Ricci, P.; Viola, E. Stress intensity factors for cracked T-sections and dynamic behaviour of T-beams. *Eng. Fract. Mech.* **2006**, *73*, 91–111. [CrossRef]
38. Cortínez, V.H.; Dotti, F.E. Mode I stress intensity factor for cracked thin-walled open beams. *Eng. Fract. Mech.* **2013**, *110*, 249–257. [CrossRef]
39. Dunn, M.L.; Suwito, W.; Hunter, B. Stress intensity factors for cracked I-beams. *Eng. Fract. Mech.* **1997**, *57*, 609–615. [CrossRef]
40. Evans, R.; Clarke, A.; Gravina, R.; Heller, M.; Stewart, R. Improved stress intensity factors for selected configurations in cracked plates. *Eng. Fract. Mech.* **2014**, *127*, 296–312. [CrossRef]
41. Müller, W.H.; Herrmann, G.; Gao, H. Elementary strength theory of cracked beams. *Theor. Appl. Fract. Mech.* **1993**, *18*, 163–177. [CrossRef]
42. Sobotka, J.C.; McClung, R.C. Stress-intensity factors solutions for straight through cracks in C-sections. *Eng. Fract. Mech.* **2022**, *271*, 108593. [CrossRef]
43. Huang, X.; Liu, Y.; Huang, X.; Dai, Y. Crack arrest behavior of central-cracked stiffened plates under uniform tensions. *Int. J. Mech. Sci.* **2017**, *133*, 704–719. [CrossRef]
44. Llopart, L.; Kurz, B.; Wellhausen, C.; Anglada, M.; Drechsler, K.; Wolf, K. Investigation of fatigue crack growth and crack turning on integral stiffened structures under mode I loading. *Eng. Fract. Mech.* **2006**, *73*, 2139–2152. [CrossRef]
45. Labeas, G.; Diamantakos, I.; Kermanidis, T. Assessing the effect of residual stresses on the fatigue behavior of integrally stiffened structures. *Theor. Appl. Fract. Mech.* **2009**, *51*, 95–101. [CrossRef]
46. Kaszynski, A. *pyansys: Python Interface to MAPDL and Associated Binary and ASCII Files*; Zenodo: Geneva, Switzerland, 2020.

47. Alshoaibi, A.M. Numerical Modeling of Crack Growth Under Mixed-Mode Loading. *Appl. Sci.* **2021**, *11*, 2975. [CrossRef]
48. Chen, F.H.K.; Shield, R.T. Conservation laws in elasticity of the J-integral type. *J. Appl. Math. Phys. (ZAMP)* **1977**, *28*, 1–22. [CrossRef]
49. Rice, J.R. A Path Independent Integral and the Approximate Analysis of Strain Concentration by Notches and Cracks. *J. Appl. Mech.* **1968**, *35*, 379–386. [CrossRef]
50. Stern, M.; Becker, E.B.; Dunham, R.S. A contour integral computation of mixed-mode stress intensity factors. *Int. J. Fract.* **1976**, *12*, 359–368. [CrossRef]
51. Yau, J.F.; Wang, S.S.; Corten, H.T. A Mixed-Mode Crack Analysis of Isotropic Solids Using Conservation Laws of Elasticity. *J. Appl. Mech.* **1980**, *47*, 335–341. [CrossRef]
52. Erdogan, F.; Sih, G.C. On the Crack Extension in Plates Under Plane Loading and Transverse Shear. *J. Basic Eng.* **1963**, *85*, 519–525. [CrossRef]
53. Ferreira, N.; Antunes, P.V.; Ferreira, J.A.M.; Costa, J.D.M.; Capela, C. Effects of Shot-Peening and Stress Ratio on the Fatigue Crack Propagation of AL 7475-T7351 Specimens. *Appl. Sci.* **2018**, *8*, 375. [CrossRef]
54. Sinclair, G.; Pieri, R. On obtaining fatigue crack growth parameters from the literature. *Int. J. Fatigue* **1990**, *12*, 57–62. [CrossRef]
55. Prasad, N.E.; Wanhill, R.J.H. (Eds.) *Aerospace Materials and Material Technologies*; Springer: Singapore, 2017; ISBN 978-981-10-2133-6.
56. Zhou, B.; Liu, B.; Zhang, S. The Advancement of 7XXX Series Aluminum Alloys for Aircraft Structures: A Review. *Metals* **2021**, *11*, 718. [CrossRef]
57. Boni, L.; Fanteria, D.; Lanciotti, A.; Lazzeri, L.; Palmiero, F.; Sollo, A. Crack propagation in flat panels stiffened by bonded pads. *Int. J. Fatigue* **2014**, *68*, 1–9. [CrossRef]